

RESEARCH ARTICLE OPEN ACCESS

OC6 Phase IV: Validation of CFD Models for Stiesdal TetraSpar Floating Offshore Wind Platform

Hannah Darling¹ | David P. Schmidt¹ | Shengbai Xie² | Jasim Sadique² | Arjen Koop³ | Lu Wang⁴ | Will Wiley⁴ | Roger Bergua Archeli⁴ | Amy Robertson⁴ | Thanh Toan Tran⁴

¹Mechanical and Industrial Engineering Department, University of Massachusetts, Amherst, Massachusetts, USA | ²Convergent Science Inc. (CSI), Madison, Wisconsin, USA | ³Maritime Research Institute Netherlands (MARIN), Wageningen, The Netherlands | ⁴National Wind Technology Center, National Renewable Energy Laboratories (NREL), Golden, Colorado, USA

Correspondence: Lu Wang (lu.wang@nrel.gov)

Received: 20 May 2024 | **Revised:** 1 November 2024 | **Accepted:** 28 November 2024

Funding: This work was supported by the National Science Foundation (2020888 and 2021693), the Dutch Ministry of Economic Affairs, and the U.S. Department of Energy Office of Energy Efficiency and Renewable Energy Wind Energy Technologies Office.

Keywords: computational fluid dynamics | experimental validation | OC6 | offshore wind energy

ABSTRACT

With only a few floating offshore wind turbine (FOWT) farms deployed anywhere in the world, FOWT technology is still in its infancy, building on a modicum of real-world experience to advance the nascent industry. To support further development, engineers rely heavily on modeling tools to accurately portray the behavior of these complex systems under realistic environmental conditions. This reliance creates a need for verification and validation of such tools to improve reliability of load and dynamic response prediction and analysis capabilities of FOWT systems. The Offshore Code Comparison Collaboration, Continued with Correlation and unCertainty (OC6) project was created under the framework of the International Energy Agency to address this need and considers a three-sided verification and validation between engineering level models, computational fluid dynamics (CFD), and experimental results. In this paper, a novel floating offshore wind platform, the Stiesdal TetraSpar, is simulated using CFD under the load conditions defined by Phase IV of the OC6 project. The comparison of these CFD results against the experimental results demonstrated the ability to predict the platform response to waves when imposing the measured wave signals as input. Although validation versus experiment was largely successful, the damping behavior was impacted by uncertainties likely originating from the mooring system and sensor umbilical cable. This extensive comparison effort with multiple CFD practitioners offers insight into best practices to achieve reliable results.

1 | Introduction

The floating offshore wind (OSW) industry is expected to play a major role in the global clean energy transition. These floating systems are particularly favorable compared to fixed as they allow access to deeper waters with more space and higher wind potential, while also minimizing public concerns for visual, noise, and environmental impacts.

However, compared to their fixed onshore/offshore counterparts, floating offshore wind turbines (FOWTs) are currently not as commercially viable, largely due to their technological immaturity, high installation and maintenance costs, and complex operating conditions. As a result, significant work is needed to optimize the design and implementation of FOWTs to reduce life cycle costs and maximize performance before they can become widespread. In particular, understanding

This is an open access article under the terms of the [Creative Commons Attribution](#) License, which permits use, distribution and reproduction in any medium, provided the original work is properly cited.

© 2024 Alliance for Sustainable Energy, LLC and The Author(s). *Wind Energy* published by John Wiley & Sons Ltd.

and predicting how these systems behave in a real-world offshore environment is critical.

FOWT systems are complex, comprising a wind turbine and control system, a floating support platform, and mooring lines anchoring the system to the sea floor. Unlike fixed-bottom platforms, FOWTs face six degrees-of-freedom (DOF) motion that is excited by the combined influence of marine environmental loads (especially wind and waves) and system restoring loads (from hydrostatics and moorings) [1]. Due to the variability and coupled nature of these forces, the resulting dynamic response and overall system loading on FOWTs is especially difficult to predict [2].

To ensure safe and efficient design, operation, and maintenance of FOWTs, understanding and predicting how these systems will behave prior to full-scale deployment is critical. Thus, a key area of research is in improving modeling techniques to simulate these complex systems in a controlled environment. Otter et al. [3] provide a comprehensive review of such modeling techniques, expanding on other reviews of physical [4–7] and numerical [8, 9] modeling approaches.

Among the numerical modeling approaches, computational fluid dynamics (CFD) plays a key role in simulating the aerodynamic and hydrodynamic interactions on FOWTs. Some recent reviews on CFD modeling of FOWTs were conducted by Xu et al. [10], Zhang et al. [11], Haider et al. [12], and Darling and Schmidt [13]. While CFD tends to be computationally demanding compared to mid-fidelity engineering models, it offers higher accuracy and can capture more aspects of the highly-integrated offshore environment with minimal assumptions [10]. However, CFD still requires validation against experimental measurements to confirm its predictive capabilities.

The Offshore Code Comparison Collaboration (OC3) through Offshore Code Comparison Collaboration, Continued with Correlation and unCertainty (OC6) projects were created under the framework of the International Energy Agency (IEA) Wind Technology Collaboration Programme to address this need for model validation [14]. This project series began

with the OC3 [15] and OC4 [16, 17] projects, under IEA Wind Tasks 23 and 30, respectively. These projects, running from 2005–2013, focused on verifying modeling tools via code-to-code comparisons of simulated responses from several different models. Following this work, the OC5 project [18–22] ran from 2014 to 2018 and focused on validating simulation results against real test data from the Alpha Ventus OSW farm. As an extension of previous Task 30 research, the OC6 project was conducted throughout 2019–2023 and included high-fidelity CFD in the validation process among engineering-level tools and measured data [23]. This project consists of four phases, focused on different aspects of FOWT design: Phase I [24–26] considers the hydrodynamic response of floating support structures, especially the nonlinear low-frequency responses, Phase II [27] considers soil/structure interaction, Phase III [28, 29] considers aerodynamic loading on a wind turbine rotor under motion, and Phase IV [30] considers full-system hydrodynamic and aerodynamic interaction. Finally, the OC7 [31] project is currently underway for 2024–2027, as part of a new Task 56.

The current paper contributes to OC6 Phase IV, focusing on benchmarking and validating models of a novel FOWT support structure [14]. The first part of this phase was discussed by Bergua et al. [30], focusing on mid-fidelity models, and the present paper extends this discussion, focusing on high-fidelity CFD. This work aims to validate the CFD results and identify best practices for achieving accurate predictions by comparing methods and results of three participating institutions.

2 | Simulation Target

OC6 Phase IV considers the coupled dynamic characteristics of the Stiesdal TetraSpar FOWT platform [32]. To determine the accuracy of the CFD results for the FOWT under hydrodynamic and aerodynamic loading, the calculated results are compared against experimental data on a 1:43 Froude-scaled model of the TetraSpar. This experimental campaign was conducted at the Harold Alfond Wind-Wave Ocean Engineering Laboratory at the University of Maine in 2018–2019 [33] and demonstrates platform responses in various controlled conditions.

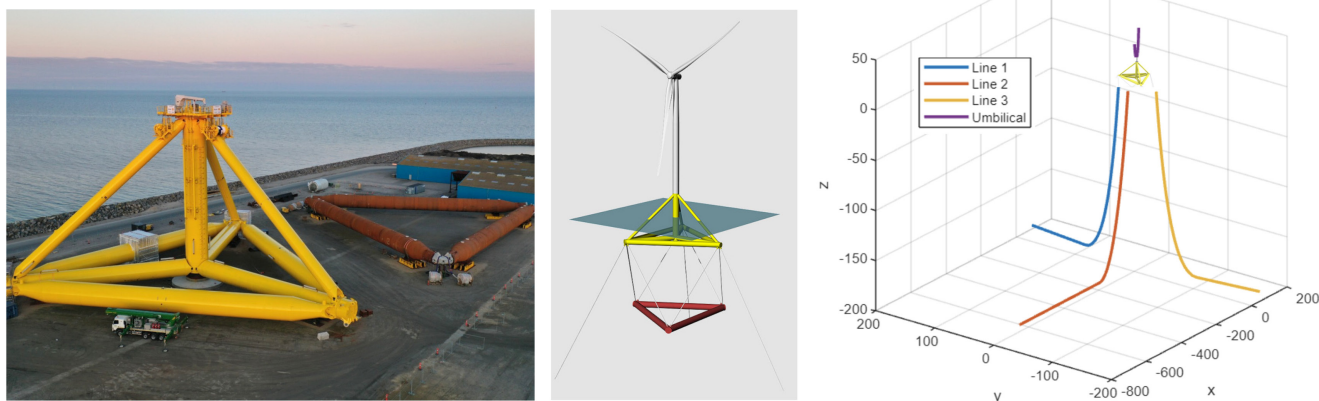


FIGURE 1 | TetraSpar full-scale platform (left) and model view (middle) used with permission from Stiesdal [32]. Also shown is the reduced-scale model's mooring layout including the sensor umbilical cable bundle used in the experimental campaign (right).

2.1 | Model Description

The TetraSpar platform (Figure 1) was designed by Stiesdal Offshore Technologies and supports a 3.6 MW Siemens Gamesa wind turbine. The TetraSpar consists of two separate structures: a tetrahedral-shaped hull supporting the tower and a triangular, high-density, hanging keel ballast. Six taut cables (keel lines) connect the two structures. A full-scale TetraSpar demonstration project was installed in Norway in 2021 and is now fully operational, but Phase IV only considers the reduced-scale model from the University of Maine experiments. Refer to Allen and Fowler [33] and Wiley et al. [34] for more information on how Froude scaling was applied to the model. Also note that the following descriptions and dimensions of the TetraSpar refer to the experimental model converted to full-scale, unless specified otherwise.

The mooring configuration of the reduced-scale model (Figure 1, right) consists of three chain catenary mooring lines with fixed anchor locations. Each line is made of a lighter upper section and a heavier lower section. The total chain length is about 700 m for the upwind line (Line 2) and about 300 m each for the two downwind lines (Lines 1 and 3) [34]. The full-scale water depth is 193.5 m. In addition to the three mooring lines, a sensor umbilical cable bundle was included to house the sensor cables and provide electrical power to the turbine during the experimental campaign and thus is also included in the numerical models for effective comparison.

The TetraSpar tower is 76 m tall and weighs $151 \cdot 10^3$ kg. For the experiments, the tower is made of aluminum and carbon fiber. The rotor-nacelle assembly (RNA) was also present in the experiments, though it was included as a lumped mass in most of the numerical simulations since the primary focus was on the hydrodynamics of the system. The total system mass is $6.08 \cdot 10^6$ kg, with the center of gravity (COG) at 39.9 m below mean water level (MWL). The origin of the system is located at the intersection of the MWL and the vertical axis of the FOWT. Wind and wave propagation is in the $+x$ direction. More detailed information, dimensions, and properties of the physical model and its components are included in the OC6 Phase IV model definition document [34] (from here on referred to as “the definition document”).

2.2 | Load Cases

OC6 Phase IV considers various system identification tests and environmental load cases (LCs) that serve to check system properties and validate the models [34].

Table 1 provides a summary of the load cases studied in this paper, including the system equilibrium (LC1.1), free decay in surge/heave/pitch (LC2.1-2.3), wind-only conditions for rated thrust considering the floating system (LC3.1) and a fixed boundary condition at the tower base (LC3.4), and wave-only conditions considering regular (LC4.1) and irregular (LC4.3) waves. Brief descriptions of each case are included in Sections 2.2.1, 2.2.2, and 2.2.3. Additional information can be found in the definition document [34].

2.2.1 | System Identification Tests

Equilibrium and static offset tests were used to assess the properties of the platform and mooring system. The test considered in this study (LC1.1) was conducted in still water conditions only under the influence of the mooring system. This test aims to verify the platform stability and equilibrium position of the modeled system.

Free decay tests (LC2.1-2.3) were also conducted to verify the calculated natural periods and hydrodynamic damping values of the FOWT system. For each case, the system was given an initial displacement (see Table 2) for the respective DOF, relative to the equilibrium position from LC1.1 [34]. Note that the blade pitch angles (90° for surge and pitch free decay and 0° for heave free decay) were selected to minimize aerodynamic contributions in the experiment’s damping results.

2.2.2 | Wind-Only Cases

The wind-only cases in this investigation (LC3.1, LC3.4) are used to examine the thrust properties of the simulated wind turbine. These tests were conducted under steady and uniform wind in still water conditions. For LC3.1, the system is floating freely in all 6-DOF and held in place by the mooring system, while in LC3.4, the platform is fixed in each DOF [34]. The fixed case serves to verify the aerodynamic loads without the influence of platform motion. Note that the tower was modeled as a rigid object in the CFD simulations.

2.2.3 | Wave-Only Cases

The wave-only cases that this study considers are two post-rated conditions, LC4.1 (regular waves) and LC4.3 (irregular waves). LC4.1 considers regular waves with a wave height of 8.31 m and a period of 12.41 s. The irregular waves in LC4.3 follow a simplified version of the Torsethaugen analytical wave spectrum, shown in Equation (1) [35]. Note that the peak enhancement factor (γ) values were customized to match the experimental model test conditions, rather than the actual Torsethaugen formulation for γ [34]

$$S(f) = \frac{H_s^2 T_p}{16} 3.26 \frac{(1 + 1.1(\ln[\gamma])^{1.19})}{\gamma} (f T_p)^{-4} e^{-(f T_p)^{-4}} \gamma e^{-\left(\frac{(f T_p - 1)^2}{2\sigma^2}\right)}, \quad (1)$$

where $S(f)$ is wave energy density (m^2/Hz), f is wave frequency (Hz), H_s is significant wave height (m), T_p is peak period (s), γ is the peak enhancement factor, and σ is the spectral width parameter (which equals 0.07 for frequencies less than the peak frequency, and 0.09 for frequencies greater than the peak frequency) [35].

3 | Numerical Methods

The TetraSpar was simulated by three groups, using three different CFD codes:

TABLE 1 | Summary of OC6 Phase IV load cases investigated using computational fluid dynamics simulations.

	Load case	Description	Wind conditions	Marine conditions	Comparison type
Static analysis	1.1	Equilibrium	None	Still water	Static response
Free decay	2.1	Surge	None	Still water	Time series ($t = 800$ s)
	2.2	Heave	None	Still water	Time series ($t = 300$ s)
	2.3	Pitch	None	Still water	Time series ($t = 500$ s)
Wind-only	3.1	Rated wind (floating)	Steady wind, $V_{hub} = 9.89$ m/s, $\Omega = 12.2$ rpm, $\beta = -6.2^\circ$	Still water	Mean response
	3.4	Rated wind (fixed)	Steady wind, $V_{hub} = 9.89$ m/s, $\Omega = 12.2$ rpm, $\beta = -6.2^\circ$	Still water	Steady response
Wave-only	4.1	Post-rated condition	None, $\Omega = 0$ rpm, $\beta = 0^\circ$	Regular waves: $H = 8.31$ m, $T = 12.41$ s	Time series ($t = 3,934$ s)
	4.3	Post-rated condition	None, $\Omega = 0$ rpm, $\beta = 0^\circ$	Irregular waves: Torsethaugen spectrum, $H_s = 8$ m, $T_p = 12.2$ s, $\gamma = 2.7$	Time series ($t = 10,977$ s)
V_{hub} : average wind speed at hub-height			H: regular wave height		H_s : significant wave height
Ω : rotor speed			T: regular wave period		T_p : peak-spectral wave period
β : blade pitch angle			t: time		γ : peak-enhancement factor

TABLE 2 | Simulation free decay matrix.

Load case	Initial position	Blade pitch set point
2.1: Surge-decay	8.77 m	90°
2.2: Heave-decay	8.59 m	0°
2.3: Pitch-decay	4.62°	90°

1. University of Massachusetts, Amherst (UMA) and Convergent Science Inc. (CSI) using CONVERGE v3.1.
2. Maritime Research Institute Netherlands (MARIN) using ReFRESKO v2.8.
3. National Renewable Energy Laboratory (NREL) using STAR-CCM+ 2306.

Methods and results from each group were compared against each other and against the experimental results. Mid-fidelity results obtained using the NREL OpenFAST [36] tool are also included for comparison of the free decay tests (LC2.1-2.3) since there are uncertainties associated with the experimental setup (see Section 4). These mid-fidelity simulations were

conducted by NREL's National Wind Technology Center. The results in the present report are obtained from an OpenFAST model slightly modified from the one reported in Bergua et al., [30] with structural flexibility disabled. This modification was done to better compare with the CFD models, which also employed rigid body assumptions. Furthermore, the number of discretization elements of the mooring lines is increased to better capture the responses of the downwind cables.

The three CFD models discussed in this report follow the general OC6 Phase IV project guidelines [34] but are also unique in terms of mesh construction, boundary conditions, and numerical models/schemes (which are summarized in Table 3 and described in more detail in the following sections).

For all groups, a digital model of the platform geometry was provided; however, some modification was required to generate suitable computational meshes due to some challenging geometric features.

- For CSI/UMA and MARIN, the sharp points at the ends of the cylindrical structures of the hull and keel are cut off at a small distance from the end. This results in a slightly smaller displacement which is compensated for by reducing

TABLE 3 | List of participating institutions and respective CFD methods.

	CSI/UMA	MARIN	NREL
CFD Software	CONVERGE v3.1 (commercial)	ReFresco v.2.8 (in-house)	STAR-CCM+ 2306 (commercial)
Load Cases Run	LC1.1, LC2.1, LC2.2, LC2.3, LC3.1, LC3.4, LC4.1, LC4.3	LC1.1, LC2.1, LC2.2, LC2.3, LC3.1, LC3.4, LC4.1, LC4.3	LC1.1, LC2.1, LC2.2, LC2.3, LC4.1
Momentum advection scheme	Second-order MUSCL with minmod flux limiter	Van Leer Harmonic TVD scheme	Hybrid second-order upwind/bounded- central differencing (Hybrid-BCD)
Pressure/velocity coupling scheme	PISO	SIMPLE	SIMPLE
Interface treatment	VOF-HRIC	ReFRICS	VOF-HRIC
Turbulence model	LES with Standard Smagorinsky, $C_s = 0.1$; Werner-Wengle model for near-wall flow	$k-\omega$ SST with Larsen correction for free surface	Spalart-Allmaras DES and all- y^+ wall treatment
Mooring Line Model	Dynamic finite-segment approach (based on lumped-mass approach) with seabed interaction	Mooring cables: dynamic anchor lines, coupled with aNySIM- XMF. Umbilical: quasi-static catenary anchor line model	Dynamic lumped-mass model for the mooring lines with coupling to MoorDyn v2. Quasi- steady catenary model for the umbilical
Rotor Model	ALM (LC3.1, LC3.4)	Blade-resolved	N/A
Mesh Type	Cartesian cut-cell	Unstructured, body-fitted mesh with arbitrary hexahedral cells	Core volume mesh generated using the trimmed cell mesher
Near Surface Refinement	Local refinements around water surface and FOWT	Volumetric refinement zones around structures	Prism-layer mesher for the near-wall mesh
Dynamic Meshing Strategy	AMR based on oct- tree refinement	Deforming and sliding mesh are used for platform motion and turbine blade rotation	Mesh morphing
Cell Count (Millions)	0.7 (LC2.1-2.3), 1.0 (LC3.1, LC3.4), 3.5 (LC4.1, LC 4.3)	10.7 (LC2.1-2.3), 16.9 (LC3.1), 5.9 (LC3.4), 10.7 (LC4.1, LC4.3)	13.6 (LC2.1-2.3), 20.7 (LC4.1)
Wave Generation	LC4.1: second-order Stokes wave theory, LC 4.3: stochastic wave generation with Equation (1)	LC4.3: experimental wave time series is reproduced via second-order wave propagation theory and iterative matching	LC4.1: first-order wave model with specified amplitude and period
Wave Absorption	Wave forcing/ relaxation zones	Wave forcing/relaxation zones	Wave forcing/ relaxation zones
Scaling of Simulations	Full-scale dimensions	Model-scale dimensions, results scaled up after	Full-scale dimensions with model-scale viscosity

the mass of the floater. For NREL, the sharp points are replaced with small partial spheres to minimize the change in displaced volume while avoiding sharp points.

- For all groups, the cylindrical structures of the hull and keel are slightly moved outwards to have a small gap between the members, thus avoiding tangent surfaces. This

may have a small influence on the added mass in heave and pitch directions.

- For all groups, the inclined cylindrical elements of the hull are extended towards and solidly joined with the center column. As this connection is above water, it has negligible influence on the hydrodynamic response.

Another important distinction between the CFD models is how the results were scaled: The CSI/UMA simulations are run at full-scale, based on the 1:43 Froude scaling; note that simulating at full-scale may have an impact on the hydrodynamic damping for these cylindrical structures. MARIN’s simulations are run at model-scale for a “model-the-model” comparison; the results are scaled up at the end using the same Froude-scaling. NREL also adopted the “model-the-model” approach, but the simulations are performed with full-scale dimensions; the viscosities of water and air are increased accordingly to match the model-scale Reynolds number.

3.1 | CSI/UMA Methods

CSI and UMA conducted the simulations using the CONVERGE v3.1 CFD software [37]. A summary of the methods used is included below and are described in more detail in Sadique et al. [38].

This CFD package uses autonomous meshing based on oct-tree refinement. The code generates the wind–wave coupled environmental flows as inflow boundary and initial conditions [39]. The wind and waves are tightly coupled using the volume-of-fluid (VOF) method. To maintain sharpness at the air–water interface, a high resolution interface capturing (HRIC) scheme is used for the fluxes at the faces of each grid cell [40]. To solve the Navier–Stokes equations (NSE), the pressure-implicit with splitting of operators (PISO) scheme is employed for pressure/velocity coupling, and large eddy simulation (LES) with a Smagorinsky turbulence model (with a constant Smagorinsky coefficient, $C_s = 0.1$) is used to represent the effects of the sub-grid scales. The dynamic Smagorinsky model was also tested but had minimal impact on the results. A second-order MUSCL scheme with the minmod flux limiter is used for advection, and the Werner–Wengle model [41] is used to model the unresolved near-wall flow around the platform.

For the wind-only cases, the turbine blades are modeled using the actuator-line model (ALM) [42]. In this model, each blade is represented by a volumeless line along which aerodynamic body forces are determined. Lift and drag contributions at each point along the lines are computed based on (1) local flow conditions

from the CFD to calculate angle of attack, α , inherently taking into account some 3D unsteady effects, and (2) airfoil data, that is, lift and drag coefficients found in XFOIL, provided in Appendix B of the definition document [34]. In general, unsteady aerodynamic effects due to dynamic stall are considered to be negligible for LC3.1, since the change in α is small as the motion of the FOWT becomes quasi-steady after the initial transient. As demonstrated by Papi et al. [43], ALM using static polars is sufficient to obtain accurate results for FOWTs when the pitching oscillation is small.

The mooring cables are modeled by a dynamic finite-segment approach, which is based on the lumped-mass approach with seabed interaction and can handle varying cable properties [44]. The dynamic response of the FOWT platform is modeled as the 6-DOF motions by the fluid–structure interaction (FSI) [38, 44].

For cases without the rotor included, the box-shaped computational domain (Figure 2) is $600 \times 227 \times 280$ m. The FOWT is located at 445 m from the inlet, and the MWL is at $z = 0$ m. Cartesian cut-cell meshing is utilized with local refinements around the water surface and platform. A base grid of $16 \times 16 \times 16$ m is used for all cases. Additional prescribed mesh refinements are embedded from 40 m below to 40 m above the MWL ($4 \times 4 \times 4$ m), around the FOWT ($4 \times 4 \times 4$ m), and at the structure surface ($0.25 \times 0.25 \times 0.25$ m). An adaptive mesh refinement (AMR) based on the instantaneous local void fraction value α is used to give a resolution of $0.5 \times 0.5 \times 0.5$ m at the air–water interface. Here, a void fraction range of $0.3 < \alpha < 0.7$ is used as the AMR criterion to provide adequate resolution at a reasonable cost. The total cell count is about 0.67 million for the free decay cases (LC2.1–2.3) and about 3.5 million for the wave-only cases (LC4.1 and LC4.3). A constant time step is used: 0.05 s for the free decay cases and 0.02 s for the wave-only cases.

In the wind-only cases (LC3.1 and LC3.4), besides the hull and keel, the geometries of the tower and nacelle are also included, and the rotor is modeled by the ALM. The domain size is increased to $1130 \times 387 \times 600$ m to reduce the numerical blockage effect which is known to affect the rotor aerodynamics. The turbine is located at $3.5D$ (where $D = 129$ m is the rotor diameter) from the inlet and $5.26D$ from the outlet. Moreover, around the turbine blades, a resolution of 2 m is generated via the AMR

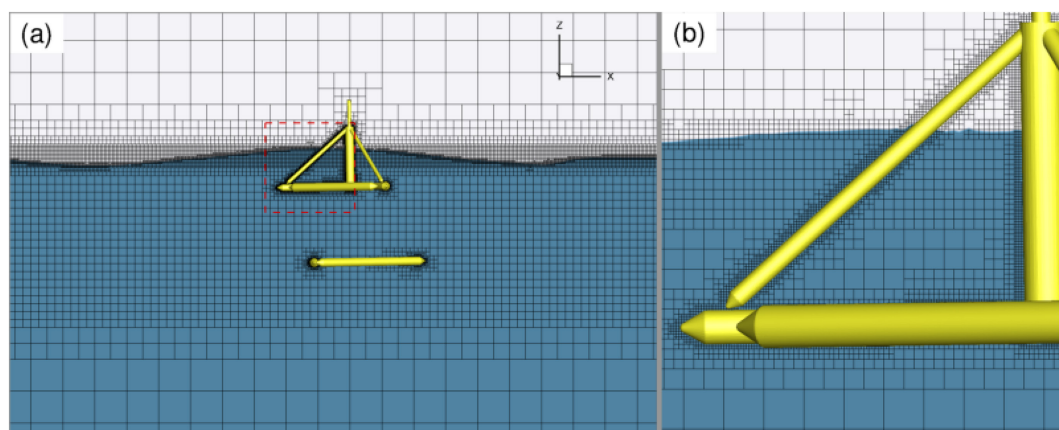


FIGURE 2 | CSI/UMA model for LC4.1 including: (a) a side view of the computational mesh and platform, (b) a zoomed-in view of the grid around the hull and free-surface.

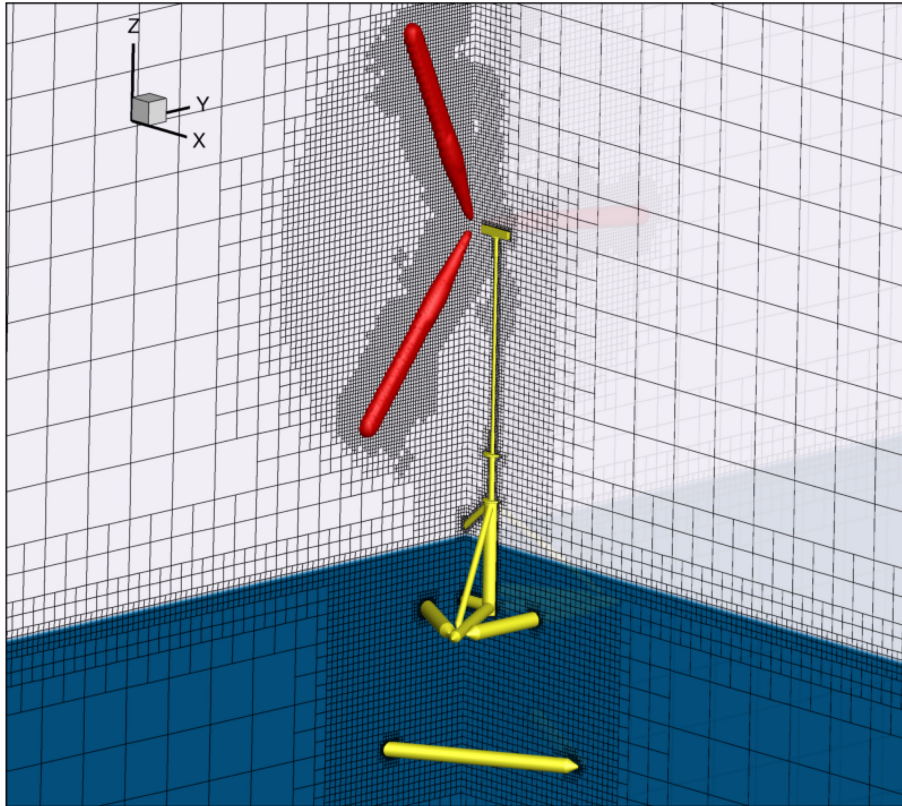


FIGURE 3 | CSI/UMA instantaneous CFD mesh for LC3.4, shown at two orthogonal cross planes. The red surfaces represent the ALM force with magnitude of 4 N/m^3 .

based on the values of ALM forces (i.e., the AMR is activated near where the magnitude of ALM force is non-zero), shown in Figure 3. To further reduce the computational cost, a coarser resolution of 1 m is used at the air–water interface, because no apparent waves are present, resulting in a total cell count of only about 1 million for these cases. Here, the time step (about 0.004 s) is restricted by the rotational speed of the turbine, only allowing the turbine to move across one CFD cell per time step.

The boundary conditions include symmetric conditions at the lateral sides, an outflow condition with atmospheric pressure at the top, no-slip wall at the bottom, and the zero-gradient Neumann condition for all variables at the outlet. Analytical waves are generated in terms of flow velocity and density distribution at the inlet where a Neumann condition is applied to the pressure. Specifically, for the regular waves in LC4.1, the second-order Stokes wave theory is used with the prescribed wave height and period, and for LC4.3, stochastic waves are generated following the provided analytical wave spectrum from Equation (1) (so the waves in LC4.3 are only the same as the experiment in a statistical sense). For the wind-only cases, a power law with an exponent of 10^{-4} is used to generate the nearly uniform wind profile.

Additionally, to prevent numerical wave reflection back into the domain, wave relaxation zones, each with a length of 200 m, are added at the inlet and outlet. The relaxation zones act as momentum and mass sinks to gradually relax the propagating waves to a prescribed condition by an exponential weighting function [45–47]. The theoretical wave condition

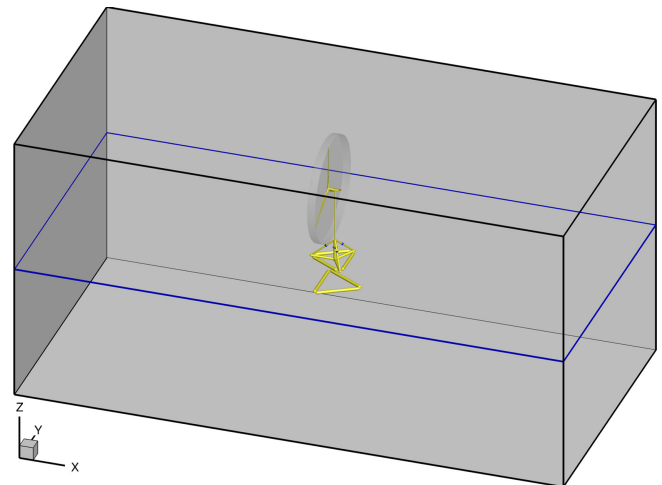


FIGURE 4 | MARIN's computational domain for the complete system. The blue line indicates the location of the free surface.

is prescribed at the inlet and the calm water condition at the outlet.

3.2 | MARIN Methods

Another set of simulations was conducted by MARIN using the CFD code ReFresco v2.8 [48]. The rectangular computational domain has side walls positioned approximately at the same distance from the FOWT as in the model tests, that is, at

4.5 m (193.5 m full-scale) with respect to the hull COG. The inlet and outlet of the domain are positioned at 9 m from the center of the platform (387 m full-scale), which is equal to three times the rotor diameter. When calculations are carried out with the hull present, the bottom of the domain is chosen at the same depth as in the model tests (4.5 m model-scale). For LC3.4, only the turbine is present in the calculations and thus the bottom of the domain is chosen at the water surface instead. The top of the domain is defined at a height of 4.5 m model-scale. The computational domain is illustrated in Figure 4 for the calculations with the complete FOWT system.

For the rotor, a blade-resolved approach is used with the provided blade geometry [34]. The nacelle geometry is schematized by a cylinder following the outline of the nacelle used in the model tests. The nose of the nacelle is chosen to be a rounded cap whereas in the model tests, no nose cap was present. It is assumed that these simplifications have little influence on the aerodynamic loading on the turbine. The tower is taken as a rigid cylinder with a slightly larger diameter as used in the model tests.

The FOWT mass properties were prescribed for each component separately, that is, for the RNA, tower, hull, keel, and umbilical. In the ReFRESKO simulations, the system was considered to be one body with a weight distribution and COG location combined from the mass and inertia properties of the separate components.

Using the time-domain code aNySIM-XMF [49], the mooring cables are modeled using dynamic anchor lines, and the umbilical was included using a quasi-static catenary anchor line model. The mooring code aNySIM-XMF is coupled to ReFRESKO through the 6-DOF equation of motion of the floater:

$$M\ddot{X} = F_H + F_{moor}, \quad (2)$$

where M denotes the 6-DOF dry mass and inertia matrix, \ddot{X} is the second-order time derivative of the state vector $X = (x, y, z, \phi, \theta, \psi)$ with $x, y, z, \phi, \theta, \psi$ representing the surge, sway, heave, roll, pitch and yaw motions, respectively. The hydrodynamic forces and moments, F_H , are calculated in ReFRESKO by solving the NSE and then integrating the solution for pressure and shear stress over the surface of the FOWT.

For the meshing strategy, an unstructured, body-fitted computational mesh with arbitrary hexahedral cells is used. Deforming mesh capabilities and sliding interfaces are utilized to account for the platform motions and turbine blade rotations. Computational grids are constructed with the grid generator software package Hexpress [50]. Volumetric refinement zones are placed around the FOWT to capture the important flow structures, such as the free surface, and local flow around the hull and turbine. The grid around the structure is refined towards the solid surfaces to capture the boundary layers. Grids are made for the following configurations:

- Hull-only inside the computational domain consisting of 5.9 million cells (Figure 5).
- Tower and stationary part of the nacelle consisting of 0.8 million cells as part of the complete computational grid for the turbine-only calculations.
- Rotor with blades and rotating part of the nacelle positioned inside a cylinder. The pitch angle of the blades are set to the pitch angle considered in the load case at hand, that is, -6.2° . The grid around the turbine consists of 9.9 million cells and is illustrated in Figure 6.
- Hull with tower, stationary part of the nacelle, and an empty cylinder at the location of the turbine rotor inside the computational domain consist of 7.0 million cells as illustrated in Figure 7 as part of the complete computational grid for the complete FOWT.

Hence, the complete grid consists of 5.9 million cells for the hull-only calculations, 10.7 million cells for the turbine-only calculations, and 16.9 million cells for the complete FOWT system.

In the ReFRESKO calculations, the harmonic total variation diminishing (TVD) scheme of van Leer is employed for the space-discretization of the momentum equations. To capture the air–water interface, ReFRICS is used [51]. To solve the NSE, the SIMPLE scheme is used for pressure/velocity coupling. The $k-\omega$ SST model is used for the turbulence model in combination with the Larsen correction for the free surface [52]. The eddy-viscosity ratio μ_T/μ is set to 1. Wall functions are used underwater as the maximum y^+ values are around 50. Above water, no wall functions are used as the maximum y^+ values are around

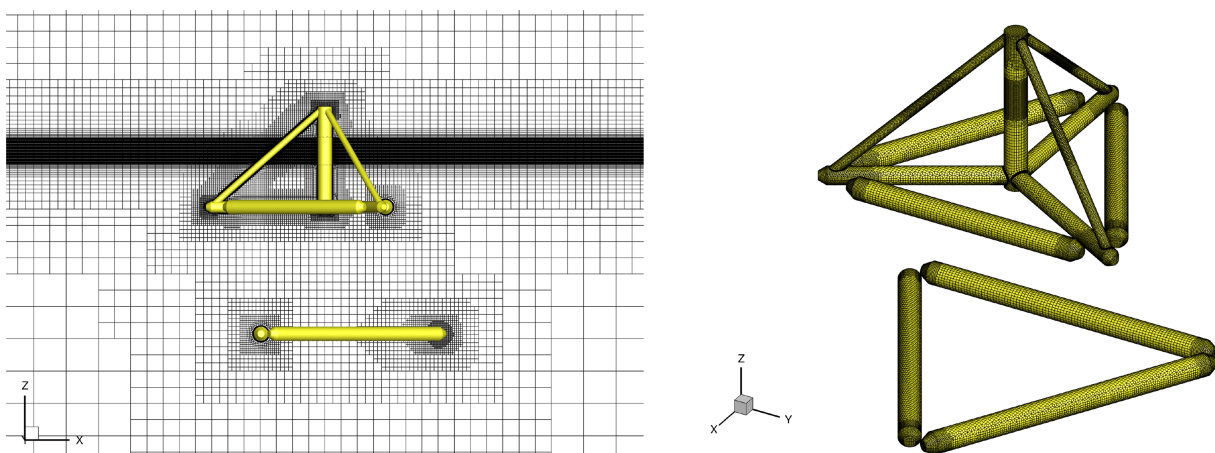


FIGURE 5 | MARIN's computational mesh around (left) and on (right) the hull and keel structures.

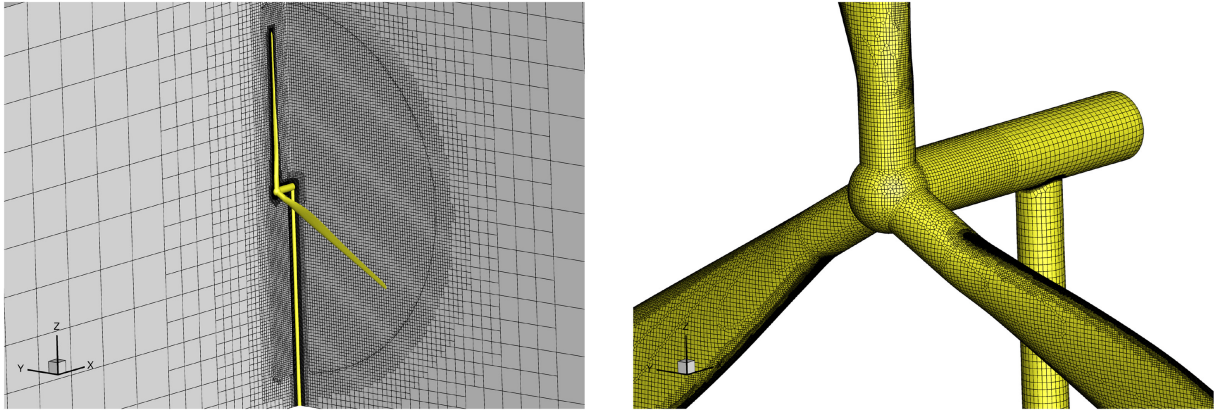


FIGURE 6 | MARIN's computational mesh around the turbine (left) and on the surface of the turbine (right).

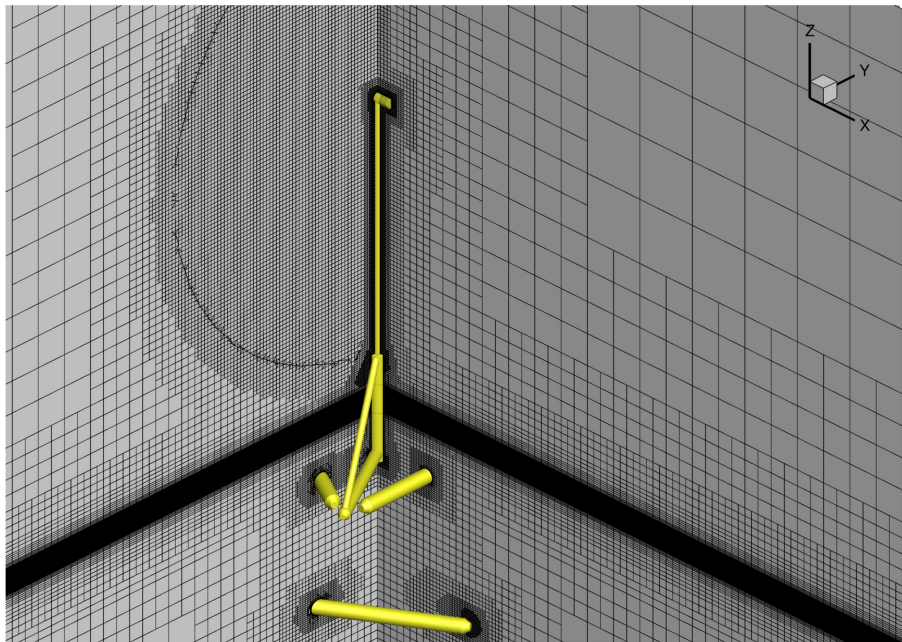


FIGURE 7 | MARIN's computational grid for the complete system including hull and turbine rotor. Note, the blades are present in this grid, but they are located behind the cutting plane.

2. The time step Δt is chosen to be $\Delta t = T_N/400$, $\Delta t = T_R/360$, or $\Delta t = T_W/400$, whichever is smallest. Here, T_N is the estimated natural period of the FOWT in surge, heave, or pitch direction, T_R is the time needed for one rotation of the turbine blades, and T_W is the wave period.

On the boundaries of the computational domain, the following conditions are imposed:

- Top surface: constant pressure condition;
- Bottom and side surfaces: free-slip wall condition;
- Inlet and outlet: a nonreflective wave boundary condition is applied with wave amplitude set to zero or the specified wave amplitude;

- For the captive turbine in wind-only conditions, a uniform inflow velocity is prescribed and a zero-gradient outflow condition is imposed.
- Surfaces of the FOWT: no-slip wall condition.

For irregular wave generation, the experimental wave time series is reproduced as closely as possible utilizing second-order wave propagation theory and an iterative matching procedure.

The turbine rotation is accounted for via sliding interfaces around the blades; the mesh inside these interfaces rotates with the turbine. Meanwhile, to account for the platform motion, a deforming mesh is used around the platform and the turbine interfaces.

During the CFD calculations, the residuals of the equations are monitored for each time step with the aim of reaching a residual level with L_2 -norm of 10^{-5} for all equations before proceeding to the next time step.

3.3 | NREL CFD Methods

The final set of CFD simulations on the TetraSpar were conducted by NREL's National Wind Technology Center, using the STAR-CCM+ 2306 CFD software [53]. NREL only conducted simulations for static equilibrium, free decay, and regular-wave LCs.

Two box-shaped computational domains of different lengths (x -direction) are used. For LC1.1-2.3 (without incident waves), the length is 600 m and for LC4.1 (with regular waves), the length is 1922.4 m (i.e., 8 wavelengths). The width and depth of both domains match those of the physical wave basin: 387 and 293.5 m, respectively. With either setup, the floater is centered in the x - and y -direction in the computational domain.

The core volume mesh is generated using the trimmed cell mesher of STAR-CCM+ in conjunction with a prism-layer mesher for the near-wall mesh. In the far field and away from the free surface, a large isotropic cell size of 13 m is specified. Near the floater, a box-shaped mesh-refinement zone encompassing both the hull and keel is included with a target isotropic cell size of 1.625 m. A second box-shaped zone encompassing only the keel refines the mesh to a target cell size of 0.8125 m. Finally, in the immediate vicinity of the structural members, cylindrical mesh-refinement zones are placed along the center-lines of the various structural members to further refine the mesh to a target cell size of approximately 0.20 m. On all surfaces of the structure, prism layer meshes with 15 layers and a total thickness of 0.48 m are generated. The thickness of the first layer is 0.003 m, resulting in a constant layer-to-layer expansion ratio of 1.29. Prism layer meshes are omitted on the outer boundaries of the domain. The mesh near and below the free surface is also refined. For LC4.1, the free surface mesh has target cell sizes of 1.6 m, 3.3 m, and 0.4 m in the x -, y -, and z -directions, respectively, across the entire domain, resulting in approximately 150

cells per wavelength and 20 cells per wave height. The cell size is gradually increased with water depth. A coarse mesh is used above water. Overall, the mesh for the shorter domain has approximately 13.6 million cells. The mesh for the longer domain for LC4.1, shown in Figure 8, has approximately 20.7 million cells. Mesh morphing is used to accommodate the motion of the structure.

For the boundaries, velocity inlet conditions are used at the inlet and outlet; the bottom and side boundaries are treated as free-slip walls, and the top boundary is a pressure outlet with extrapolated backflow direction. For LC4.1, the incident waves are generated based on the first-order wave model with the specified wave amplitude and period from Table 1. The wave-field velocity and volume fraction are prescribed on the inlet and outlet boundaries. Wave-forcing/relaxation zones with a length of two wavelengths are placed next to the inlet and outlet boundaries to prevent the reflection of radiated and diffracted waves.

The two-phase flow is modeled using the VOF formulation. Turbulence is modeled with the Spalart–Allmaras detached eddy simulation and all- y^+ wall treatment [53, 54]. To solve the NSE, the SIMPLE scheme is used with 20 iterations per time step for pressure/velocity coupling. A hybrid second-order upwind/bounded-central differencing (Hybrid-BCD) scheme, the HRIC scheme, and second-order upwinding are, respectively, used for the advection of momentum, volume fraction, and the turbulence variable (modified diffusivity). Also, an implicit second-order (backward differencing) time scheme is used. A fixed time step is used for all simulations. The size of the time step depends on the load case. LC1.1 uses a large time step of 0.1 s. All free decay simulations (LC2.1-2.3) use a time step of 0.05 s. LC4.1 (regular waves) uses a time step of 0.0375 s (approximately 330 steps per wave period).

Since NREL did not run any aerodynamic cases, the rotor and tower are not modeled in the CFD simulations. The mooring lines are modeled by coupling to the dynamic lumped-mass mooring solver MoorDyn v2 [55]. The umbilical cable in the air is modeled quasi-statically using the catenary line model of STAR-CCM+. FSI is based on an implicit algorithm for coupling

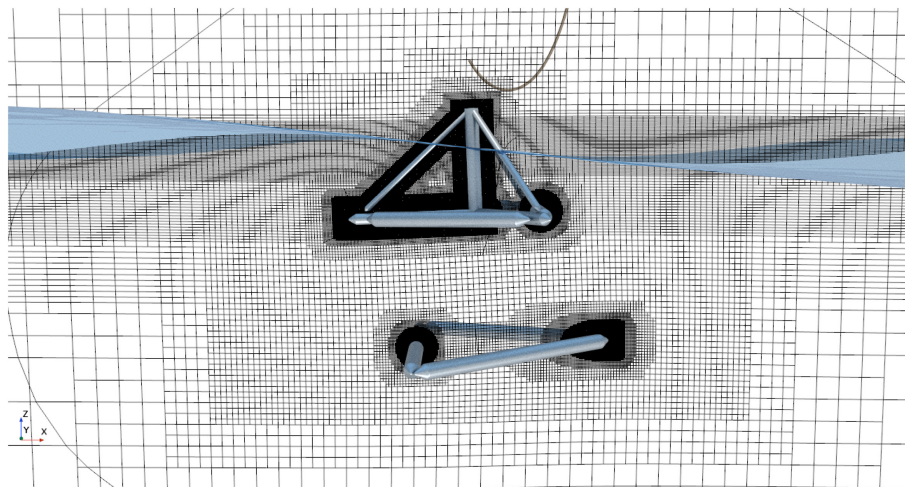


FIGURE 8 | NREL's CFD mesh for LC4.1 in the vicinity of the platform.

fluid flow and body motion that updates mesh morphing at each iteration within a time step [53].

4 | Results and Discussion

In this section, results and discussions are presented for the LCs described in Table 1, including system identification tests, wind-only cases, and wave-only cases. The results for each model are labeled as follows:

- *CSI/UMA*: Convergent Science Inc. and the University of Massachusetts, Amherst (CONVERGE, CFD)
- *MARIN*: Maritime Research Institute Netherlands (ReFRESKO, CFD)
- *NREL*: National Renewable Energy Laboratory (STAR-CCM+, CFD)
- *NREL-OF*: National Renewable Energy Laboratory (OpenFAST)

For most LCs, the numerical model results are compared against the University of Maine experiments. Due to the lack of repeats available for these experimental runs, confidence intervals could not be computed formally. Only LC4.1 and LC4.3 have repeat experiments available, for which uncertainty is represented in the results via a shaded region encapsulating all experimental runs.

4.1 | System Identification Tests

To confirm the properties of the platform and mooring system, equilibrium (LC1.1) and free decay (LC2.1-2.3) tests were

conducted in still water conditions on the moored platform without wind or wave loading. In the equilibrium CFD calculations, the system did not yet reach a static offset position within the calculation duration provided by each group. Therefore, the offsets for these datasets were calculated by averaging over the last three periods (two periods for sway) of the time series for the respective DOF. The periods used are based on the full-scale system natural frequencies from the definition document [34] (see Table 4). The equilibrium positions determined by this analysis were subtracted from the reported results in the remaining LCs for a more direct comparison.

From the LC1.1 test, the numerical models are consistent with the physical system in terms of the hull pitch equilibrium position. The experimental model faced a hull pitch rotation of -1.99° [34], and all three CFD models were within 0.25° of this value: The equilibrium hull pitch rotation was -2.08° for CSI/UMA, -1.74° for MARIN, and -1.94° for NREL.

For the free decay tests (Figures 9–12), the system was given an initial displacement (see Table 2) relative to the LC1.1 equilibrium position for the respective DOF: surge (LC2.1), heave (LC2.2), or pitch (LC2.3). Note that during the free decay tests in the experimental campaign, the surge resting position of the system was located 14m upwind (at full-scale) relative to the origin. The exact reason for this difference in position is unknown but could be attributed to the sensor umbilical cable, the exact shape and location of the mooring lines on the basin floor, and the friction between the moorings and floor [30]. This effect likely impacts the restoring stiffness of the moorings and adds uncertainty to the experimental results. Refer to Bergua et al. [30] for more information on the uncertainties present in the experimental results.

TABLE 4 | Full-scale natural frequencies and respective periods calculated from UMaine experiment.

	Roll	Pitch	Yaw	Surge	Sway	Heave
Natural frequency (Hz)	0.029	0.030	0.007	0.0073	0.0044	0.025
Natural period (s)	34.48	33.33	142.86	136.99	227.27	40

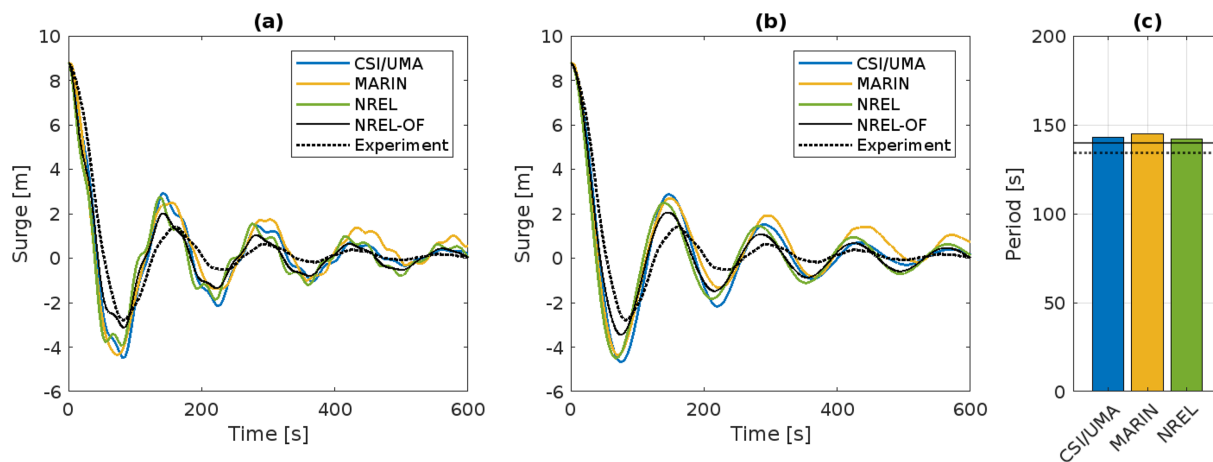


FIGURE 9 | LC2.1 surge free decay results, including (a) the original time series, (b) time series with new reference point, and (c) period. The colored bars represent the numerical results, the dashed black line represents the experimental result, and the solid black line represents the OpenFAST result.

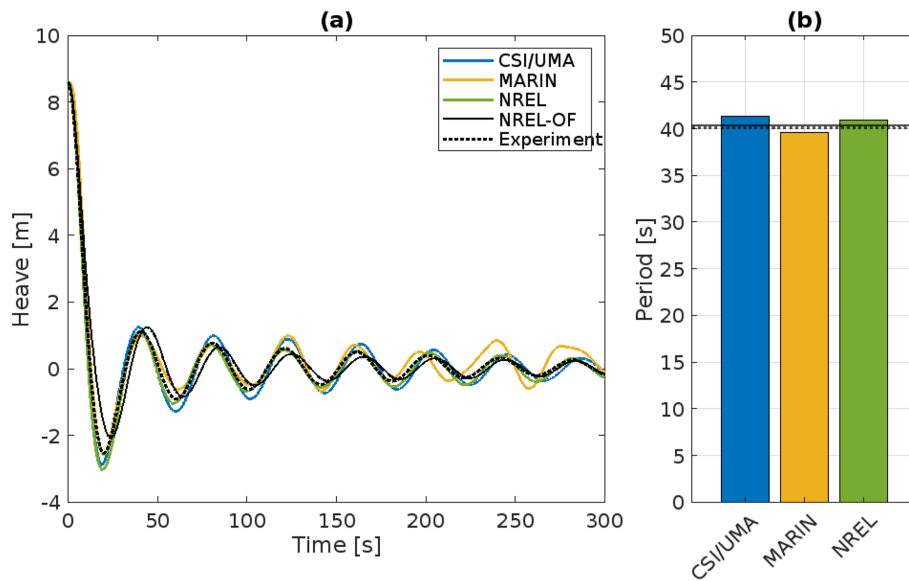


FIGURE 10 | LC2.2 heave free decay results, including (a) the time series plot and (b) period. The colored bars represent the numerical results, the dashed black line is the experimental result, and the solid black line is the OpenFAST result.

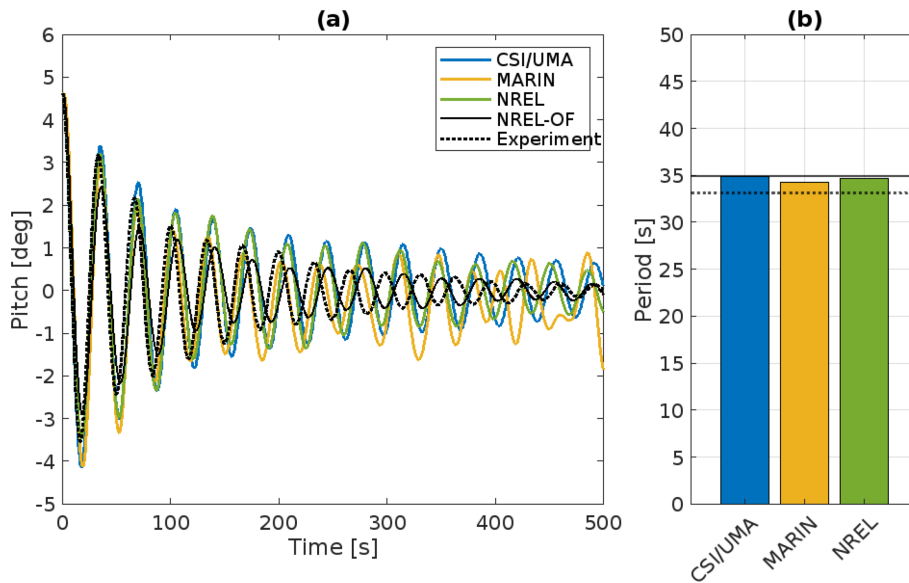


FIGURE 11 | LC2.3 pitch free decay results, including (a) the time series plot and (b) period. The colored bars represent the numerical results, the dashed black line is the experimental result, and the solid black line is the OpenFAST result.

Figures 9–11 show the free decay time series and period for surge (LC2.1), heave (LC2.2), and pitch (LC2.3), respectively. In the time series plots, there is an apparent coupling between the different DOFs, which is particularly noticeable in Figure 9a (LC2.1), as there are multiple frequencies visible in the time series. The lower frequency corresponds to the surge natural frequency, while the higher frequencies come from other platform motions (primarily pitch). Note that this coupling is less visible in the experimental time series. Furthermore, in the MARIN datasets, some coupling between the different modes of motion can also be observed in LC2.2 (Figure 10) and LC2.3 (Figure 11) that results in increasing motion response during the simulation.

To account for the coupling seen in LC2.1, the point of reference was shifted vertically downward from the hull COG until the frequency component associated with pitch motion was minimized, to produce the signal shown in Figure 9b. The periods reported in Figures 9c–11c were then computed by averaging the duration between consecutive peaks/troughs of the respective signal. Note that the periods determined for the experiment closely match the expected natural periods from Table 4. The periods of the numerical simulations, including OpenFAST, match well with the experiment for heave but are slightly higher than the experiment for surge and pitch (likely due to the uncertainties associated with the sensor umbilical cable in the experiment).

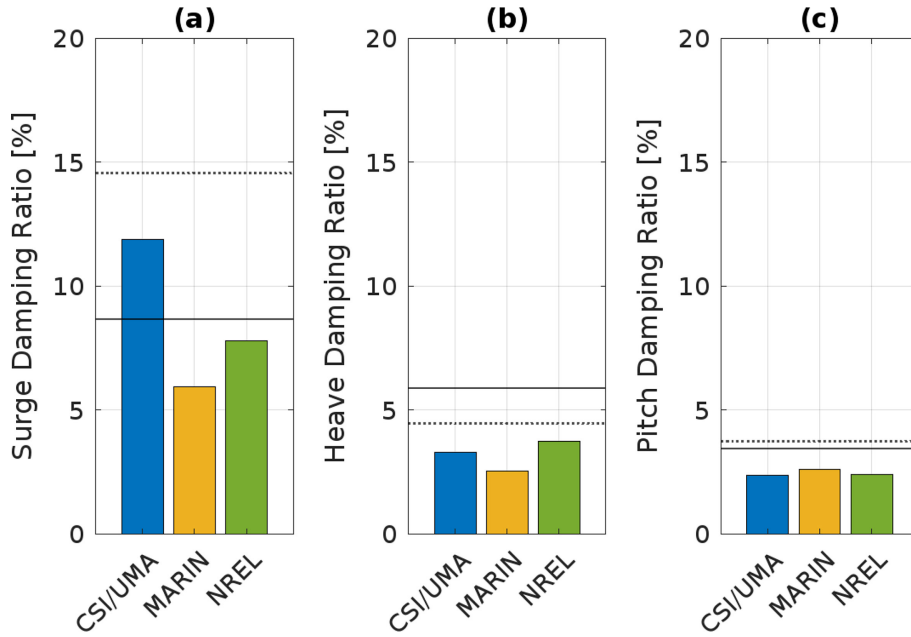


FIGURE 12 | Damping ratio results for (a) LC2.1-surge, (b) LC2.2-heave, and (c) LC2.3-pitch. The colored bars represent the numerical results, the dashed black lines are the experimental results, and the solid black lines are the OpenFAST results.

Damping ratios for each case (Figure 12) were calculated based on the logarithmic decrement approach described in Bergua et al. [56]. In this approach, the logarithmic decrement (δ) and then the damping ratio (ζ) are calculated from the difference in amplitude between consecutive peaks in the decay via Equations (3) and (4).

$$\delta = \ln \frac{x(t)}{x(t+T)}, \quad (3)$$

$$\zeta = \frac{\delta}{\sqrt{(2\pi)^2 + \delta^2}}, \quad (4)$$

where $x(t)$ is the amplitude of the peak at time t and $x(t+T)$ is the amplitude of the next peak, one period (T) away. The damping ratios are calculated for each consecutive cycle along the decay (for both the positive and negative peaks) and are then averaged to yield the results in Figure 12. Note that the damping ratio results are subject to some uncertainty due to their dependence on the chosen data (i.e., the range and number of peaks) for analysis. For example, the present analysis skips the first period and uses all peaks in the next two periods for LC2.1 or the next four periods for LC2.2/LC2.3.

As seen in the damping ratio results, the experiment faced more damping compared to the numerical results in the surge direction. In the heave direction, the numerical damping ratios are relatively close to that calculated from the experimental data, although NREL-OF shows higher damping than the other cases. For the pitch motion, the damping ratio from NREL-OF is close to that of the experiment as a result of directly tuning to the experimental measurements, but the CFD models predict a lower value. Variations between the CFD models may be attributed to differences in the numerical set-up, for example, mesh resolution and mooring/umbilical cable solvers.

The higher damping observed from the experiment, especially in the surge and pitch directions, is likely caused by the additional energy dissipation from the contact between the basin floor and the mooring chains. The friction between the chains and the tank bottom is not modeled in the numerical simulations. Furthermore, the repeated lifting and dropping of the chain on the tank bottom can also induce additional energy dissipation that is likely not accurately captured by the numerical models.

4.2 | Wind-Only Cases

LC3.1 and LC3.4 focus on the system responses under steady uniform wind loading and with still water conditions. CFD results for these cases were only collected for CSI/UMA and MARIN and are compared against the experimental data. In LC3.1, the system is free-floating (subject to 6-DOF motions) with the mooring lines holding it in place. In LC3.4, the system is not subject to any platform motions.

Figure 13 includes the results for the relative hull pitch and fairlead tensions for LC3.1. The former is calculated from the participants' reported results, subtracting the equilibrium offset condition from LC1.1. The fairlead tensions correspond to the loads for each of the respective mooring lines at the point where they connect to the platform. Fairlead 2 is the upwind mooring line, and fairleads 1 and 3 are the two downwind lines, as depicted in Figure 1. Figure 14 compares the average aerodynamic rotor thrust for the floating (LC3.1) versus fixed (LC3.4) platform. Note that the aerodynamic rotor thrust for the experiment was not measured, so for comparison, the thrust was estimated based on the tower base bending moment measurements from LC3.1 considering rigid body motion and disregarding the influence of the umbilical cables (see Bergua et al. [30] for a more detailed explanation of how this force was calculated).

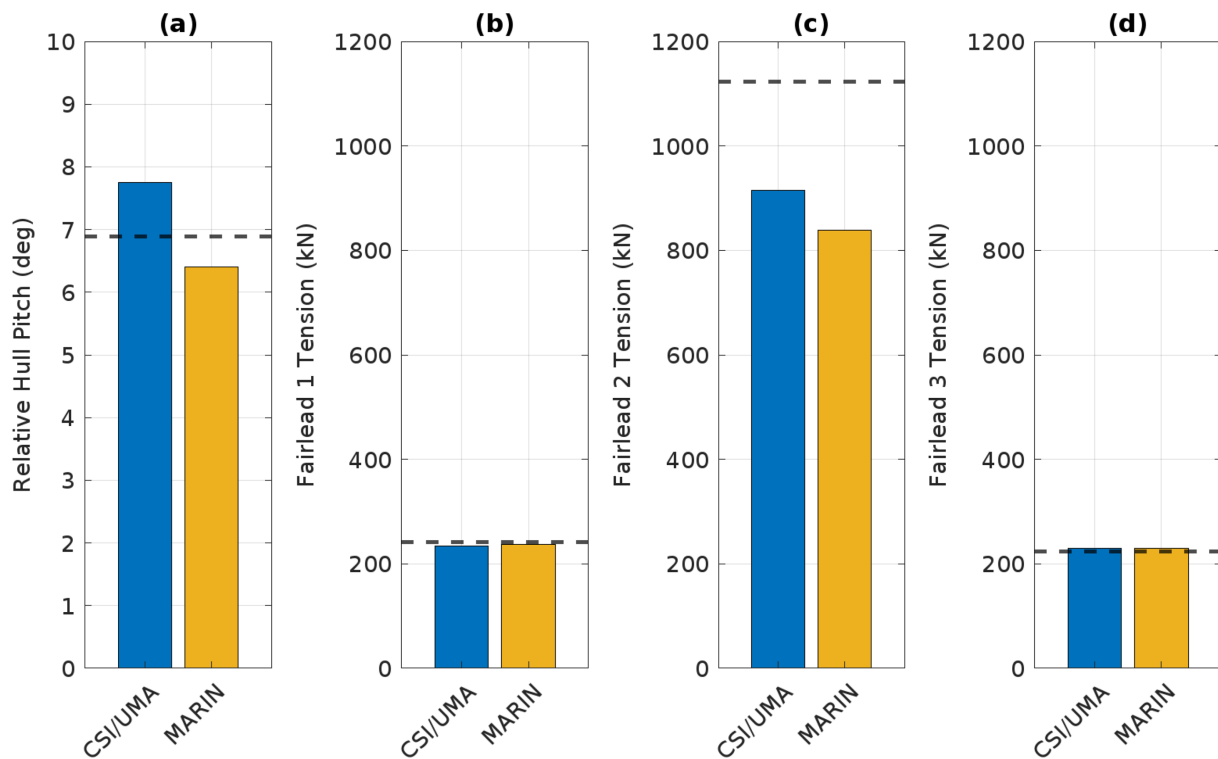


FIGURE 13 | LC3.1 results for (a) relative hull pitch, (b) fairlead 1 tension, (c) fairlead 2 tension, and (d) fairlead 3 tension, with colored bars representing numerical results and dashed black lines representing experimental results.

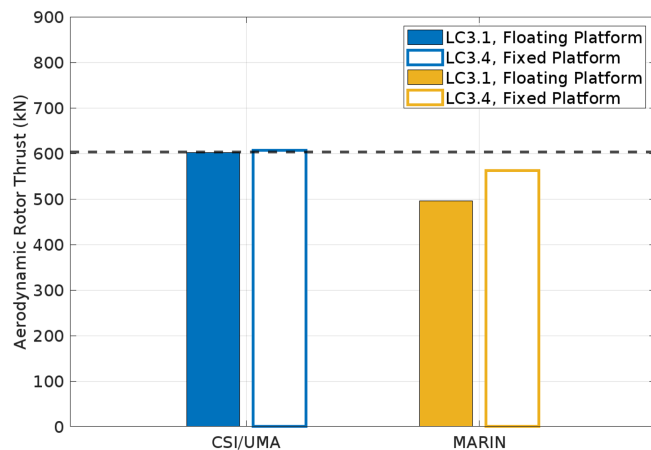


FIGURE 14 | Average aerodynamic rotor thrust for LC3.1 and LC3.4. The dashed black line represents the estimation from the experimentally measured bending moment from LC3.1. An estimation of the experimental thrust force is not available for LC3.4, but it is expected that the thrust should be similar to LC3.1 for small platform pitch angles.

This estimation of 603 kilonewtons (kN) is included in Figure 14 with a dashed black line. The actual thrust force is expected to be slightly lower than this approximated value when the tower flexibility is considered due to the lever arm distance contributions in tower and RNA weights with regard to the tower base.

The CFD results for fairlead 1 and 3 tensions (Figure 13b,d) match closely with the experimental results. However, for fairlead 2 (Figure 13c), the CFD simulations predict a lower tension than observed in the experiment. According to the

previous OC6 Phase IV report [30], this difference is likely because the experiment has a large initial surge offset in resting conditions prior to applying the wind load. The MARIN results show a lower tension (839 kN) than CSI/UMA (915 kN), due to the lower aerodynamic rotor thrust that MARIN predicted (see Figure 14). The thrust for CSI/UMA is around 600 kN for LC3.1, while MARIN's prediction is around 500 kN. This difference likely attributes to the use of different rotor modeling approaches between MARIN and CSI/UMA: MARIN adopted a blade-resolved CFD approach, while CSI/UMA uses the ALM approach.

For the relative hull pitch (Figure 13a), the CFD models are both within 1° of the experimental value, with MARIN predicting a slightly lower value and CSI/UMA predicting a slightly higher value. Recall that the equilibrium hull pitch rotation from LC1.1 was -1.99° for the experiment, -2.08° for CSI/UMA, and -1.74° for MARIN. When rated wind conditions are applied in LC3.1, the relative pitch rotation for the experiment, CSI/UMA, and MARIN are 6.90° , 7.74° , and 6.40° , respectively.

For both LC3.1 and LC3.4, the aerodynamic rotor thrust for CSI/UMA matches closely with the estimated value, at around 600 kN. The results for MARIN are slightly lower than this value at 495 kN for LC3.1 and 562 kN for LC3.4, again likely due to MARIN using a different rotor model than CSI/UMA. At present, the reason for the difference in turbine thrust between LC3.1 and L3.4 in MARIN's results is unclear. One hypothesis is that at these low Reynolds numbers, the blade-resolved thrust results are sensitive to the larger blade pitch angle relative to the incoming flow when the platform is floating.

4.3 | Wave-Only Cases

LC4.1 and LC4.3 focus on the system responses under regular and irregular wave-only conditions, respectively, without wind loading. For LC4.3, CFD results were only collected for CSI/UMA and MARIN.

To compare the results for LC4.1, response amplitude operators (RAOs) were calculated. The RAOs are the ratios of the response amplitudes (i.e., surge, heave or pitch motion) at the wave frequency (around 0.081 Hz) to the incident wave amplitude. Both the response amplitudes and the wave amplitude at the wave frequency are estimated from fast Fourier transforms [30]. The first 300 s of the time series were removed from each dataset to remove transient effects. Figure 15 shows the RAOs for surge, heave, and pitch for each numerical model compared to the average RAOs from the three experimental runs.

For the surge RAO (Figure 15a), the MARIN results match the experimental result well, while the other models predict higher values. For heave (Figure 15b), the CSI/UMA simulation predicts a lower value than the experiment, while the other models predict slightly higher values. Finally, for pitch (Figure 15c), MARIN matches the experimental results closely, while the others predict slightly lower values.

With the wave frequency of LC4.1 being far from any resonance frequency of the system, it is reasonable to expect that the system damping has limited impact on the motion RAOs. Therefore, the differences between the numerical results and the measurements are most likely a consequence of the small differences in geometry and numerical set-up, uncertainties in the system mass properties, and the characterization of the moorings and umbilical.

For LC4.3 (irregular waves), the results are compared using power spectral densities (PSDs) of the wave elevation (Figure 16a–c) as well as the hull surge, heave, and pitch motions (Figure 17). These PSDs were computed using the Welch method [57, 58]. In this analysis, the signal is divided into segments with 90% overlap. Hamming windowing is used on each segment, with a frequency resolution of 0.002 Hz, corresponding to a window length of 500 s. The mean value is subtracted from each signal to remove the peak at 0 Hz, so that the energy at low frequencies is visible. Ideally, when showing the PSD, all datasets should have the same duration for a direct comparison. However, the CFD simulations were not run for the full 10,977 s intended for this LC due to time and resource limitations: the CSI/UMA simulations have 3,300 s of data and the MARIN simulations have 630 s. Therefore, the two codes are compared separately against the experimental dataset, which was truncated to be the same duration as the respective CFD result. From this comparison, the signals with shorter duration appear to show more fluctuation in the frequency spectrum, both in the experimental results and in the CFD results.

This fluctuation in the frequency spectrum is most noticeable in Figures 16b and 17d–f where the MARIN results are compared with the experimental results for the first 630s. In these figures, it can be observed that MARIN’s PSD results are in close agreement with the experimental results. This agreement is due to MARIN’s effort in matching the wave time series in the simulation with the experiment as described in Section 3.2.

In each PSD, a clear peak is apparent near the wave frequency (around 0.081 Hz). Although fluctuation is present in some cases, both CFD models are able to capture this peak frequency. A PSD integral can be calculated to characterize the level of response

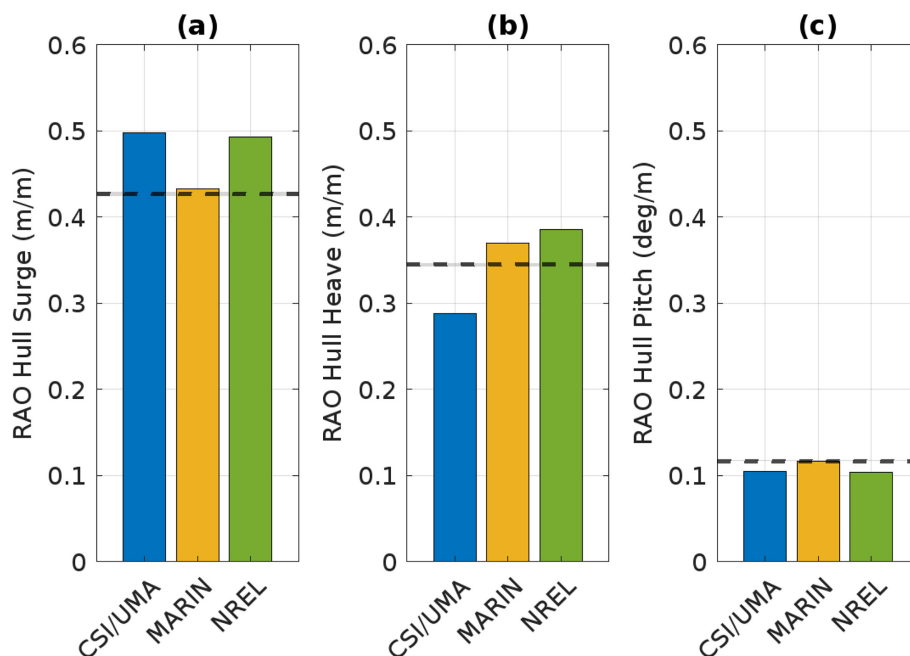


FIGURE 15 | LC4.1 RAO results for (a) surge, (b) heave, and (c) pitch, with colored bars representing numerical results and a dashed black line representing the average of three experimental runs. A shaded gray region encapsulates all experimental runs. Note the gray region is very thin since the repeated experimental runs are nearly identical.

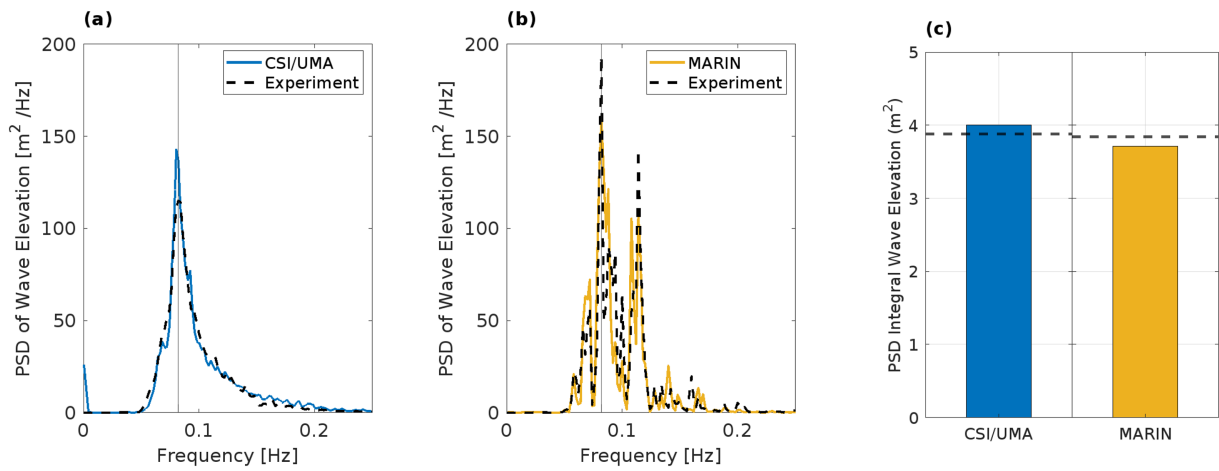


FIGURE 16 | Comparison of LC4.3 wave elevation PSD from (a) CSI/UMA and (b) MARIN to the experimental measurements and (c) the PSD Integral for the 0.046–0.25 Hz range. Colored lines/bars represent the numerical results and dashed black lines represent the experimental results. Note that only one experimental run is available for the experimental wave elevation, so uncertainty is not accounted for.

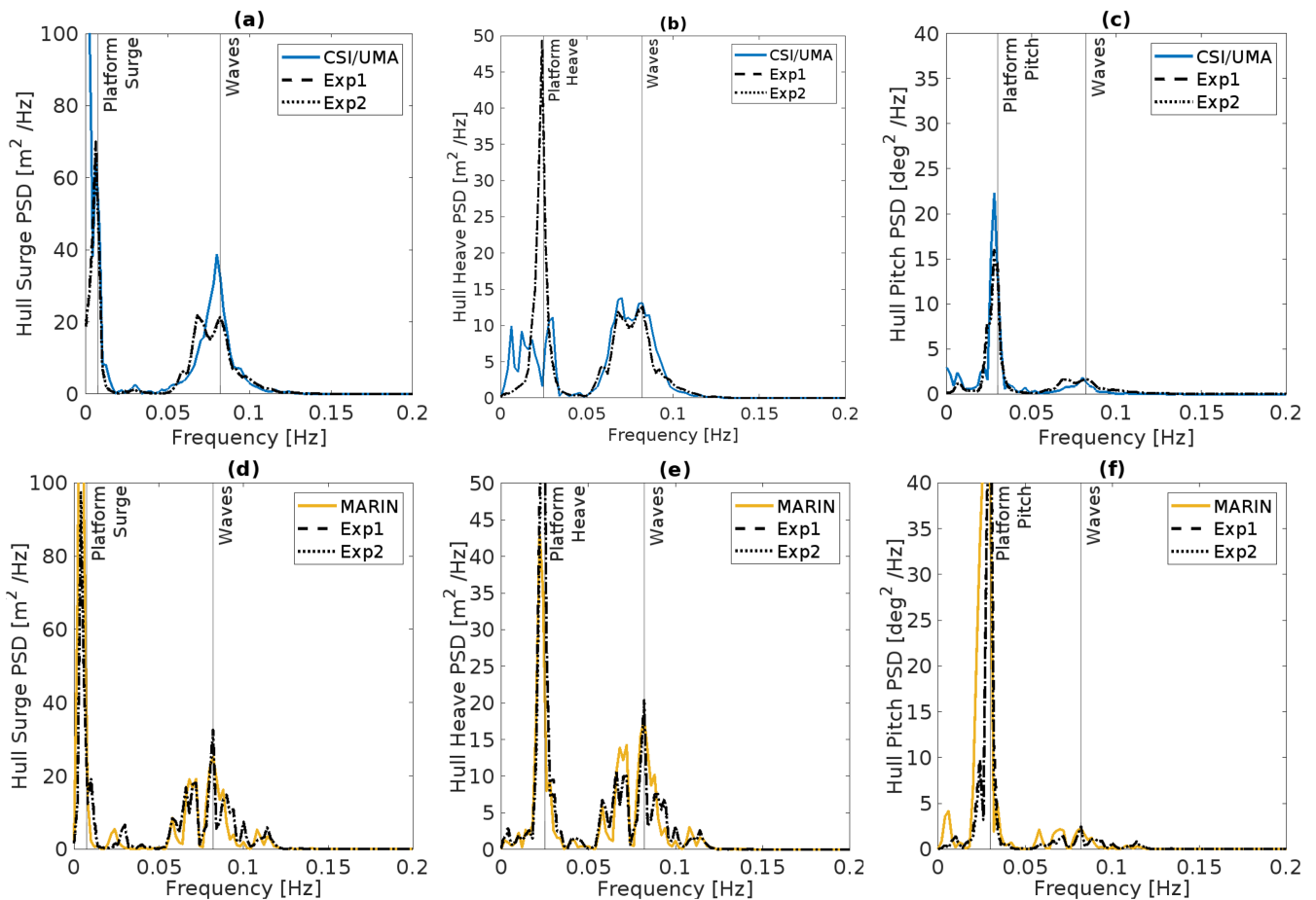


FIGURE 17 | LC4.3 PSD results for (a/d) surge, (b/e) heave, and (c/f) pitch with vertical gray lines at motion natural frequencies and the wave-peak frequency. Note that there were two experimental runs for this load case.

over a given frequency range of interest, shown in Figures 16c and 18. To calculate the PSD integral, the area under the PSD curve is determined for the frequency range of 0.046–0.25 Hz for the wave elevation plots and 0.046–0.15 Hz for the surge, heave, and pitch plots, corresponding to the linear wave excitation region. This calculation is equivalent to the variance over the

specified frequency range and is correlated with fatigue loading [30].

In terms of the wave elevation results, MARIN imposes incoming waves that closely follow the experimental wave time series, while the CSI/UMA model generates stochastic waves according to the

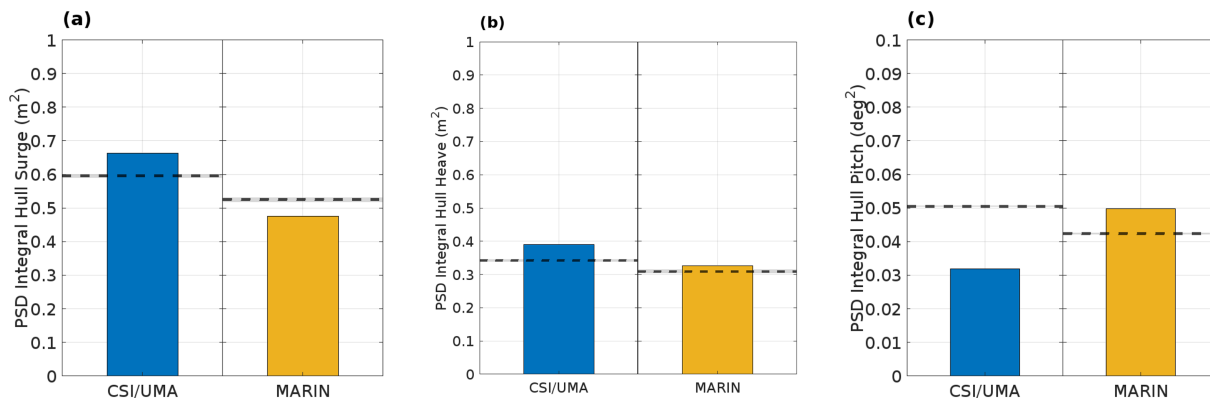


FIGURE 18 | LC4.3 PSD integral results for 0.046-0.15Hz range for (a) surge, (b) heave, and (c) pitch, with colored bars representing numerical results and dashed black lines representing the average of 2 experimental runs. Note that the gray region is very thin since the experimental runs are nearly identical.

theoretical spectrum of Equation (1). Both techniques offer reasonable results shown in the PSDs and PSD integral in Figure 16. In the PSDs for hull surge, heave, and pitch, an additional peak can be observed at the platform natural frequency for the respective DOF. MARIN is able to capture the energy at these peaks for all three cases well. CSI/UMA captures the peaks at the surge and pitch natural frequencies fairly well, but wider energy spreading is observed near the heave natural frequency for which the reason is still unknown and further investigation is needed. From the comparison of wave time series and platform response, it appears that the best agreement with experimental results can be obtained if the input wave time series to the CFD calculations is matched as closely as possible with the experimental wave time series. This finding is consistent with the findings of Robertson et al. from OC6 Phase I [24], in which the wave realization techniques affected the ability to replicate the measured waves.

5 | Conclusions

In support of the OC6 Phase IV project, participants from the University of Massachusetts Amherst, Convergent Science Inc, the Maritime Research Institute Netherlands, and the National Renewable Energy Laboratory used CFD modeling approaches to investigate the TetraSpar FOWT platform motion response under various environmental loading conditions. To validate the CFD results, a comparison was made against experimental measurements collected at the University of Maine. Another key objective of this work is to provide insight into the capability and accuracy of state-of-the-art CFD modeling techniques to predict the loading on, and the dynamic response of, a FOWT platform.

One key finding from this investigation is that the CFD models were able to predict the freedecay periods well compared to the experimental results. However, in the experiments, much higher damping levels were observed than obtained with the CFD simulations. This is likely due to additional energy dissipation originating from the interaction of the mooring lines with the basin floor that was not included in the numerical models. There are also some uncertainties associated with the sensor umbilical cable in the experimental campaign that may affect these results. Additionally, the postprocessing of the free decay

results is complicated due to the presence of multiple frequencies in the decay signals, particularly for the case of surge decay motion. To account for this coupling, the point of reference was vertically shifted downward from the hull COG until the pitch frequency response was minimized.

From the wind-only cases, there was no observed benefit in using the blade-resolved approach over ALM for modeling the rotor. For the current problem, ALM is a pragmatic option since the results produced with this approach match well with the experimental results. The blade-resolved approach is more complex to set up and is computationally more expensive due to higher mesh requirements (refer to Table 3).

For the motion response in waves, the CFD models had good predictive capabilities for LC4.1 (regular waves), with small discrepancies between the various CFD results and experimental results that can likely be attributed to CFD modeling differences and experimental uncertainties. In the context of irregular waves (LC4.3), the CFD results generally predicted the platform responses well at the wave peak frequency, but challenges emerged when evaluating the low-frequency responses corresponding to the surge, heave, and pitch natural frequencies. This limitation may be attributed to differences in wave realization and how accurately the groups replicate the measured waves. MARIN appears to better capture the low-frequency responses compared to CSI/UMA likely because MARIN uses an input wave time series that is very similar to the experimental wave time series, while CSI/UMA generates stochastic waves following the analytical spectrum. The latter could make the results more susceptible to statistical uncertainty. Accurate replication of the experimental wave time series is necessary for direct comparison.

The high cost of detailed CFD simulations requires accurate results to justify the required effort. Though most of the computational predictions matched well with the experimental results, the ability to accurately predict system response in the low frequency range, near the natural frequencies, differs greatly between codes. These discrepancies may be sensitive to the irregular wave realization strategies. The limits on resolution imposed by computational cost may be another factor limiting accuracy. An additional area of interest is the damping

differences between model-scale and full-scale simulations. Subsequent research will investigate the details of surge/pitch coupling in the computational results (i.e., for free decay) and novel ways of analyzing the computational data to systematically produce noncoupled results.

Author Contributions

H. Darling: formal analysis, data curation, writing—original draft, writing—review and editing, visualization. **D.P. Schmidt:** writing—original draft, writing—review and editing, supervision. **S. Xie:** methodology, software, investigation, writing—original draft, writing—review and editing. **J. Sadique:** methodology, software, writing—original draft, writing—review and editing. **A. Koop:** methodology, software, investigation, writing—original draft, writing—review and editing. **L. Wang:** methodology, software, investigation, writing—original draft, writing—review and editing. **W. Wiley:** methodology, investigation, writing—review and editing. **R. Bergua:** methodology, formal analysis, investigation, writing—review and editing. **A. Robertson:** conceptualization, supervision, project administration, funding acquisition. **T. Tran:** software.

Acknowledgments

The authors acknowledge the TetraSpar Demonstrator ApS and shareholders Shell, RWE Renewables, TEPCO RP, and Stiesdal Offshore Technologies. The University of Massachusetts Amherst acknowledges that this research is supported in part by the National Science Foundation grants 2020888 and 2021693. Additionally, Convergent Science provided CONVERGE licenses and technical support for this work. MARIN acknowledges that their work was partly funded by the Dutch Ministry of Economic Affairs. This work was authored in part by the National Renewable Energy Laboratory, operated by Alliance for Sustainable Energy, LLC, for the U.S. Department of Energy (DOE) under Contract No. DE-AC36-08GO28308. Funding provided by the U.S. Department of Energy Office of Energy Efficiency and Renewable Energy Wind Energy Technologies Office. The views expressed in the article do not necessarily represent the views of the DOE or the U.S. Government. The U.S. Government retains and the publisher, by accepting the article for publication, acknowledges that the U.S. Government retains a nonexclusive, paid-up, irrevocable, worldwide license to publish or reproduce the published form of this work, or allow others to do so, for U.S. Government purposes. A portion of this research was performed using computational resources sponsored by the U.S. Department of Energy's Office of Energy Efficiency and Renewable Energy and located at the National Renewable Energy Laboratory.

Conflicts of Interest

The authors declare no conflicts of interest.

Data Availability Statement

Data from this project will be made available to the public through the US Department of Energy Data Archive and Portal, <https://doi.org/10.21947/2179225> [59].

References

1. M. Barooni, T. Ashuri, D. Velioglu Sogut, S. Wood, and S. Ghaderpour Taleghani, "Floating Offshore Wind Turbines: Current Status and Future Prospects," *Energies* 16, no. 1 (2023): 2.
2. D. Matha, M. Schlipf, R. Pereira, and J. Jonkman, "Challenges in Simulation of Aerodynamics, Hydrodynamics, and Mooring-Line Dynamics of Floating Offshore Wind Turbines," in *The Twenty-First*

International Offshore and Polar Engineering Conference (Maui, HI: ISOPE, 2011).

3. A. Otter, J. Murphy, V. Pakrashi, A. Robertson, and C. Desmond, "A Review of Modelling Techniques for Floating Offshore Wind Turbines," *Wind Energy* 25, no. 5 (2022): 831–857.

4. S. Gueydon, I. Bayati, and E. J. de Ridder, "Discussion of Solutions for Basin Model Tests of FOWTs in Combined Waves and Wind," *Ocean Engineering* 209 (2020): 107288.

5. K. Müller, F. Sandner, H. Bredmose, J. Azcona, A. Manjock, and R. Pereira, "Improved Tank Test Procedures for Scaled Floating Offshore Wind Turbines," in *International Wind Engineering Conference* (Stockholm, Sweden: IWEC Foundation, 2014).

6. A. N. Robertson, J. M. Jonkman, A. J. Goupee, et al., "Summary of Conclusions and Recommendations Drawn From the DeepCwind Scaled Floating Offshore Wind System Test Campaign," in *ASME 2013 32nd International Conference on Ocean, Offshore and Arctic Engineering*, Vol. 8: Ocean Renewable Energy (Nantes, France: ASME, 2013), V008T09A053.

7. G. Stewart and M. Muskulus, "A Review and Comparison of Floating Offshore Wind Turbine Model Experiments," *Energy Procedia* 94 (2016): 227–231.

8. M. Atcheson, A. Garrad, L. Cradden, et al., *Floating Offshore Wind Energy: The Next Generation of Wind Energy*, eds. J. Cruz and M. Atcheson (Cham, Switzerland: Springer International Publishing, 2016).

9. A. Cordle and J. Jonkman, "State of The Art in Floating Wind Turbine Design Tools," in *The Twenty-first International Offshore and Polar Engineering Conference* (Maui, HI: ISOPE, 2011).

10. S. Xu, Y. Xue, W. Zhao, and D. Wan, "A Review of High-Fidelity Computational Fluid Dynamics for Floating Offshore Wind Turbines," *Journal of Marine Science and Engineering* 10, no. 10 (2022): 1357.

11. W. Zhang, J. Calderon-Sanchez, D. Duque, and A. Souto-Iglesias, "Computational Fluid Dynamics (CFD) Applications in Floating Offshore Wind Turbine (FOWT) Dynamics: A Review," *Applied Ocean Research* 150 (2024): 104075.

12. R. Haider, X. Li, W. Shi, Z. Lin, Q. Xiao, and H. Zhao, "Review of Computational Fluid Dynamics in the Design of Floating Offshore Wind Turbines," *Energies* 17, no. 17 (2024): 4269.

13. H. Darling and D. P. Schmidt, "The Role of Fully Coupled Computational Fluid Dynamics for Floating Wind Applications: A Review," *Energies* 17, no. 19 (2024): 4836.

14. IEA Wind TCP, "Task 30: Offshore Code Comparison Collaboration, Continuation, With Correlation and Uncertainty," (2018), <https://iea-wind.org/task30/>.

15. J. Jonkman and W. Musial, "Offshore Code Comparison Collaboration (OC3) for IEA Task 23 Offshore Wind Technology and Deployment," NREL/TP-5000-48191 (Golden, CO: National Renewable Energy Lab. (NREL), 2010).

16. W. Popko, F. Vorpahl, A. Zuga, et al., "Offshore Code Comparison Collaboration Continuation (OC4), Phase 1 - Results of Coupled Simulations of an Offshore Wind Turbine With Jacket Support Structure," in *The Twenty-Second International Offshore and Polar Engineering Conference* (Rhodes, Greece: ISOPE, 2012).

17. A. Robertson, J. Jonkman, W. Musial, F. Vorpahl, and W. Popko, "Offshore Code Comparison Collaboration, Continuation: Phase II Results of a Floating Semisubmersible Wind System," in *EWEA Offshore 2013* (Frankfurt, Germany: EWEA, 2013).

18. W. Popko, M. L. Huhn, A. N. Robertson, et al., "Verification of a Numerical Model of the Offshore Wind Turbine From the Alpha Ventus Wind Farm Within OC5 Phase III," in *ASME 2018 37th International Conference on Ocean, Offshore and Arctic Engineering*, Vol. 10: Ocean Renewable Energy (Madrid, Spain: ASME, 2018), V010T09A056.

19. W. Popko, A. Robertson, J. Jonkman, et al., "Validation of Numerical Models of the Offshore Wind Turbine From the Alpha Ventus Wind Farm Against Full-Scale Measurements Within OC5 Phase III," in *ASME 2019 38th International Conference on Ocean, Offshore and Arctic Engineering*, Vol. 10: Ocean Renewable Energy (Glasgow, Scotland, UK: ASME, 2019), V010T09A065.
20. A. N. Robertson, F. Wendt, J. M. Jonkman, et al., "OC5 Project Phase Ib: Validation of Hydrodynamic Loading on a Fixed, Flexible Cylinder for Offshore Wind Applications," *Energy Procedia* 94 (2016): 82–101.
21. A. N. Robertson, F. Wendt, J. M. Jonkman, et al., "OC5 Project Phase II: Validation of Global Loads of the DeepCwind Floating Semisubmersible Wind Turbine," *Energy Procedia* 137 (2017): 38–57.
22. A. N. Robertson, F. F. Wendt, J. M. Jonkman, et al., "OC5 Project Phase I: Validation of Hydrodynamic Loading on a Fixed Cylinder," in *The Twenty-fifth International Offshore and Polar Engineering Conference* (Kona, HI: ISOPE, 2015).
23. US Department of Energy Wind Energy Technologies Office, "IEA Research Study Extended to Improve Accuracy of Offshore Wind Systems Design Tools: Floating and Fixed-Bottom Structures Can Benefit From Further Design Optimization," (2018), <https://www.energy.gov/eere/wind/articles/iea-research-study-extended-improve-accuracy-offshore-wind-systems-design-tools>.
24. A. N. Robertson, S. Gueydon, E. Bachynski, et al., "OC6 Phase I: Investigating the Underprediction of Low-Frequency Hydrodynamic Loads and Responses of a Floating Wind Turbine," *Journal of Physics: Conference Series* 1618 (2020): 032033.
25. L. Wang, A. Robertson, J. Jonkman, et al., "OC6 Phase Ia: CFD Simulations of the Free-Decay Motion of the DeepCwind Semisubmersible," *Energies* 15, no. 1 (2022): 389.
26. L. Wang, A. Robertson, J. Jonkman, et al., "OC6 Phase Ib: Validation of the CFD Predictions of Difference-Frequency Wave Excitation on a FOWT Semisubmersible," *Ocean Engineering* 241 (2021): 110026.
27. R. Bergua, A. Robertson, J. Jonkman, et al., "OC6 Phase II: Integration and Verification of a New Soil–Structure Interaction Model for Offshore Wind Design," *Wind Energy* 25, no. 5 (2022): 793–810.
28. R. Bergua, A. Robertson, J. Jonkman, et al., "OC6 Project Phase III: Validation of the Aerodynamic Loading on a Wind Turbine Rotor Undergoing Large Motion Caused by a Floating Support Structure," *Wind Energy Science* 8, no. 4 (2023): 465–485.
29. S. Cioni, F. Papi, L. Pagamonci, et al., "On the Characteristics of the Wake of a Wind Turbine Undergoing Large Motions Caused by a Floating Structure: An Insight Based on Experiments and Multi-Fidelity Simulations From the OC6 Project Phase III," *Wind Energy Science* 8, no. 11 (2023): 1659–1691.
30. R. Bergua, A. Robertson, J. Jonkman, D. Alarcón Fernández, and P. Trubat Casal, "OC6 Project Phase IV: Validation of Numerical Models for Novel Floating Offshore Wind Support Structures," *Wind Energy Science* 9, no. 4 (2024): 1025–1051.
31. IEA Wind TCP, "IEA Wind TCP Task 56: OC7 Project (Offshore Code Comparison Collaboration 7)," (2024), <https://iea-wind.org/task-56-oc7-project-offshore-code-comparison-collaboration-7/>.
32. Stiesdal, "The TetraSpar Full-Scale Demonstration Project," (2021), <https://www.stiesdal.com/offshore/the-tetraspar-full-scale-demonstration-project/>.
33. C. Allen and M. Fowler, "1/43rd Scale Basin Testing of the 3.6 MW TetraSpar Floating Offshore Wind Turbine – Spar Configuration," Advanced Structures and Composites Center, University of Maine, Report No. 19-25-1720 (Orono, ME, USA, 2019).
34. W. Wiley, R. Bergua, A. Robertson, et al., "Definition of the Stiesdal Offshore Tetraspar Floating Wind System for OC6 Phase IV," NREL/TP-5700-86442, National Renewable Energy Laboratory (NREL), (Golden, CO, 2023).
35. K. Torsethaugen and S. Haver, "Simplified Double Peak Spectral Model for Ocean Waves," in *The Fourteenth International Offshore and Polar Engineering Conference* (Toulon, France: ISOPE, 2004).
36. J. Jonkman and M. Sprague, "NREL Wind Research, Openfast," (Golden, CO: National Renewable Energy Lab. (NREL), 2023), <https://www.nrel.gov/wind/nwtc/openfast.html>.
37. K. J. Richards, P. K. Senecal, and E. Pomraning, "CONVERGE v3.1.," (Madison, WI: Convergent Science, 2023), <https://convergecd.com/products/converge-cfd-software>.
38. J. Sadique, S. Xie, Y. S. Shekhawat, H. Darling, and D. P. Schmidt, "Numerical Assessment and Validation of Floating Offshore Wind Turbines in One Fully Coupled CFD Simulation," (paper presented at the Offshore Technology Conference Asia, Kuala Lumpur, Malaysia, OTC-34956-MS, 2023).
39. H. Johlas, "Simulating the Effects of Floating Platforms, Tilted Rotors, and Breaking Waves for Offshore Wind Turbines," (Doctoral diss., University of Massachusetts, Amherst, 2021).
40. T. Waclawczyk and T. Koronowicz, "Modeling of the Wave Breaking With CICSAM and HRIC High Resolution Schemes," in *ECCOMAS CFD: Proceedings of the European Conference on Computational Fluid Dynamics* (Egmond aan Zee, The Netherlands: ECCOMAS, 2006).
41. H. Werner and H. Wengle, "Large-Eddy Simulation of Turbulent Flow Over and Around a Cube in a Plate Channel," in *Turbulent Shear Flows 8: Selected Papers from the Eighth International Symposium on Turbulent Shear Flows, Munich, Germany, September 9–11, 1991* (Berlin, Heidelberg: Springer, 1993), 155–168.
42. J. N. Sorensen and W. Z. Shen, "Numerical Modeling of Wind Turbine Wakes," *Journal of Fluids Engineering* 124, no. 2 (2002): 393–399.
43. F. Papi, J. Jonkman, A. Robertson, and A. Bianchini, "Going Beyond BEM With BEM: An Insight Into Dynamic Inflow Effects on Floating Wind Turbines," *Wind Energy Science* 9, no. 5 (2024): 1069–1088.
44. S. Xie and J. Sadique, "CFD Simulations of Two Tandem Semi-Submersible Floating Offshore Wind Turbines Using a Fully-Coupled Fluid-Structure-Interaction Simulation Methodology," in *ASME 2022 4th International Offshore Wind Technical Conference* (Boston, MA: ASME, 2022), V001T01A006.
45. A. P. Engsig-Karup, H. B. "Unstructured Nodal DG-FEM Solution of High-Order Boussinesq-Type Equations," Technical University of Denmark (Doctoral diss., Kgs. Lyngby, Denmark, 2006).
46. D. R. Fuhrman, P. A. Madsen, and H. B. Bingham, "Numerical Simulation of Lowest-Order Short-Crested Wave Instabilities," *Journal of Fluid Mechanics* 563 (2006): 415–441.
47. N. G. Jacobsen, D. R. Fuhrman, and J. Fredsøe, "A Wave Generation Toolbox for the Open-Source CFD Library: OpenFOAM®," *International Journal for Numerical Methods in Fluids* 70, no. 9 (2012): 1073–1088.
48. P. Crepier, "ReFRESCO: Versatile Solver, Tailored for Maritime Challenges," (2023), <https://www.marin.nl/en/about/facilities-and-tools/software/refresco>.
49. V. Schaap, "ANYSIM XMF," (2023), <https://www.marin.nl/en/about/facilities-and-tools/software/anysim>.
50. NUMECA, "NUMECA: Pre-Processing and Meshing Solutions," (2023), <https://www.numeca.de/en/products-meshing-solutions/>.
51. C. M. Klaij, M. Hoekstra, and G. Vaz, "Design, Analysis and Verification of a Volume-of-Fluid Model With Interface-Capturing Scheme," *Computers and Fluids* 170 (2018): 324–340.
52. B. E. Larsen and D. R. Fuhrman, "On the Over-Production of Turbulence Beneath Surface Waves in Reynolds-Averaged Navier-Stokes Models," *Journal of Fluid Mechanics* 853 (2018): 419–460.

53. Siemens, “Simcenter STAR-CCM+ CFD Software,” (2024), <https://plm.sw.siemens.com/en-US/simcenter/fluids-thermal-simulation/star-cm/>.
54. P. Spalart, W.-H. Jou, M. Strelets, and S. Allmaras, “Comments on the Feasibility of LES for Wings, and on a Hybrid RANS/LES,” in *Advances in DNS/LES* (Columbus, OH: Greyden Press, 1997), 137–147.
55. M. Hall, “Moordyn V2: New Capabilities in Mooring System Components and Load Cases,” in *ASME 2020 39th International Conference on Ocean, Offshore and Arctic Engineering*, Vol. 9: Ocean Renewable Energy, (ASME, 2020), V009T09A078.
56. R. Bergua, A. Robertson, J. Jonkman, and A. Platt, “Specification Document for OC6 Phase II: Verification of an Advanced Soil-Structure Interaction Model for Offshore Wind Turbines,” NREL/TP-5000-79938 (Golden, CO: National Renewable Energy Lab. (NREL), 2021).
57. M. H. Hayes, *Statistical Digital Signal Processing and Modeling* (Hoboken, NJ: John Wiley & Sons, 1996).
58. P. Stoica and R. Moses, *Spectral Analysis of Signals* (Upper Saddle River, NJ: Pearson Prentice Hall, 2005).
59. A. Robertson and R. Bergua, “OC6 Project Phase IV: Validation of Numerical Models for Novel Floating Offshore Wind Support Structures,” US Department of Energy [dataset], (2024), <https://doi.org/10.21947/2179225>.